Author(s): Boraei, Ahmed T. A.; Haukka, Matti; Sarhan, Ahmed A. M.; Soliman, Saied M.; Al-Majid, Abdullah Mohammed; Barakat, Assem

Title: Synthesis of C2-Symmetrical Bis-(β-Enamino-Pyran-2,4-dione) Derivative Linked via 1,6-Hexylene Spacer: X-ray Crystal Structures, Hishfeld Studies and DFT Calculations of Mono- and Bis-(Pyran-2,4-diones) Derivatives

Year: 2021

Version: Published version

Please cite the original version:

Boraei, A. T. A., Haukka, M., Sarhan, A. A. M., Soliman, S. M., Al-Majid, A. M., & Barakat, A. (2021). Synthesis of C2-Symmetrical Bis-(β-Enamino-Pyran-2,4-dione) Derivative Linked via 1,6-Hexylene Spacer: X-ray Crystal Structures, Hishfeld Studies and DFT Calculations of Mono- and Bis-(Pyran-2,4-diones) Derivatives. Symmetry, 13(9), Article 1646. https://doi.org/10.3390/sym13091646

symmetry

MDPI

Article

Synthesis of C_2-Symmetrical *Bis*-(β-Enamino-Pyran-2,4-dione) Derivative Linked via 1,6-Hexylene Spacer: X-ray Crystal Structures, Hishfeld Studies and DFT Calculations of Mono- and *Bis*-(Pyran-2,4-diones) Derivatives

Ahmed T. A. Boraei [1,*], Matti Haukka [2], Ahmed A. M. Sarhan [3], Saied M. Soliman [4], Abdullah Mohammed Al-Majid [5] and Assem Barakat [5,*]

1 Chemistry Department, Faculty of Science, Suez Canal University, Ismailia 41522, Egypt
2 Department of Chemistry, University of Jyväskylä, P.O. Box 35, FI-40014 Jyväskylä, Finland; matti.o.haukka@jyu.fi
3 Chemistry Department, Faculty of Science, Arish University, Al-Arish 45511, Egypt; ahmed_sarhan252@yahoo.com or asarhan@aru.edu.eg
4 Department of Chemistry, Faculty of Science, Alexandria University, P.O. Box 426, Ibrahimia, Alexandria 21321, Egypt; saied1soliman@yahoo.com or saeed.soliman@alexu.edu.eg
5 Department of Chemistry, College of Science, King Saud University, P.O. Box 2455, Riyadh 11451, Saudi Arabia; amajid@ksu.edu.sa
* Correspondence: ahmed_tawfeek83@yahoo.com or ahmed_boraei@science.suez.edu.eg (A.T.A.B.); ambarakat@ksu.edu.sa (A.B.); Tel.: +966-11467-5901 (A.B.); Fax: +966-11467-5992 (A.B.)

check for updates

Citation: Boraei, A.T.A.; Haukka, M.; Sarhan, A.A.M.; Soliman, S.M.; Al-Majid, A.M.; Barakat, A. Synthesis of C_2-Symmetrical *Bis*-(β-Enamino-Pyran-2,4-dione) Derivative Linked via 1,6-Hexylene Spacer: X-ray Crystal Structures, Hishfeld Studies and DFT Calculations of Mono- and *Bis*-(Pyran-2,4-diones) Derivatives. *Symmetry* **2021**, *13*, 1646. https://doi.org/10.3390/sym13091646

Academic Editors: Rui Tamura, György Keglevich and Sergei D. Odintsov

Received: 27 July 2021
Accepted: 4 September 2021
Published: 7 September 2021

Publisher's Note: MDPI stays neutral with regard to jurisdictional claims in published maps and institutional affiliations.

Abstract: The synthesis of C_2-symmetrical *bis*(β-enamino-pyran-2,4-dione) derivative **3** connected via 1,6-hexylene linker was reported for the first time. X-ray structures and Hirshfeld studies of the new *bis*- β-enamino-pyran-2,4-dione derivative **3** along with two structurally related pyran-2,4-dione derivatives **2a,b** were discussed. A comparative analysis of the different intermolecular contacts affecting the crystal stability was presented. Generally, the H . . . H, O . . . H, and H . . . C interactions are common in all compounds and are considered the most abundant contacts. In addition, DFT calculations were used to compute the electronic properties as well as the ^{1}H and ^{13}C NMR spectra of the studied systems. All compounds (except **3**) are polar where **2a** (3.540 Debye) has a higher dipole moment than **2b** (2.110 Debye). The NMR chemical shifts were calculated and excellent correlations between the calculated and experimental data were obtained (R^2 = 0.93–0.94).

Keywords: pyran-2,4-dione; C_2-symmetrical; Hirshfeld analysis; AIM; DFT; intramolecular hydrogen bond

1. Introduction

Pyrone and its analogs have been in the focus of organic chemists due to their wide range of interesting chemical properties, in addition to many biological and therapeutic applications [1–3]. They are considered as good synthons in a number of synthetic transformations, especially the ones leading to natural products heterocyclic systems isolated from fungi, bacteria, insects, animals, plants, and marine organisms that possess a wide range of pharmaceutical actions such as phytotoxic, neurotoxic, cytotoxic, antifungal, and anti-biotic activities [4]. Several representative examples were isolated from the nature and pyrone scaffolds have been found in their chemical structures such as Nectriapyrone A&B, Nocapyrone G, Griseulin, Wailupemycin A&F, Phaechromycin B, Nigerapyrone A&B, Neurymenolide A, Decaturin A&B, (+)-Violapyrone, and others [5–18].

Pyrone scaffold and related analogs have multi-functional groups such as enone, ester group, and conjugated diene which can serve as versatile building blocks for the synthesis of numerous target molecules [3]. Thus, development of a highly efficient synthetic protocol affording pyrone scaffold under mild conditions has become of considerable attention

for researchers. Several approaches have been reported in the literature, including the microwave method [19] and many transition metal-mediated methods [3,20,21] for the synthesis of pyrone moiety. On the other hand, some important investigations have been carried out and reported recently on the synthesis and spectroscopic behavior of pyrone scaffold [22–25].

Symmetry plays a crucial role in many human activities such as in the sciences and arts. It engages in chemical reactions, reagents, and catalysts to enhance the selectivity of the synthesis of chemical compounds. Symmetry has been employed in diverse areas, including design processes, mathematics as a problem-solving tool, physical laws, and in many domains of chemistry in which it can be utilized for solving chemical problems. To design and construct symmetrical structures is still a challenge.

In view of these encouraging reports, and in line with our interest to develop the chemistry of pyrone derivatives, the aim of the present work was to synthesize a new C_2-symmetrical *bis*(*β*-enamino-pyran-2,4-dione) derivative **3** linked by 1,6-hexylene spacer and shed the light on its molecular and supramolecular structure aspects with the aid of X-ray crystal structure, Hirshfeld, and DFT calculations. Additionally, comparative structural analyses were performed with the two previously reported structures **2a,b** shown in Scheme 1.

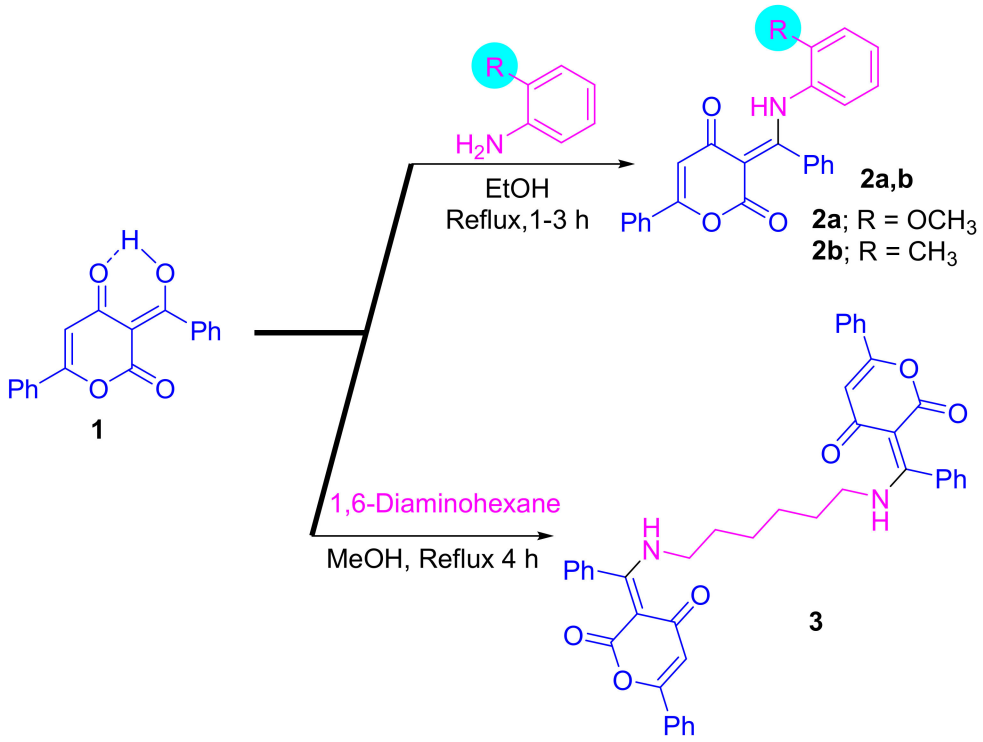

Scheme 1. Synthesis of *β*-enamino-pyran-2,4-diones derivative **2a,b** and C_2-symmetrical *bis*(*β*-enamino-pyran-2,4-dione) derivative **3**.

2. Materials and Methods

General

"Melting-point apparatus (SMP10) was used to measure the melting points of the synthesized compounds in open capillaries and uncorrected. The reaction progress was monitored chromatographically by thin-layer (TLC) and UV light was used for spot detection. Bruker AC 400 MHz spectrometer was used for nuclear magnetic resonance (^{1}H- and ^{13}C-NMR) recording in $CDCl_3$ solvent and the presence of internal standard (tetramethylsilane). Chemical shifts were represented in δ (ppm) and coupling constants are given in Hz. Flash EA-1112 instrument was used for elemental analysis determination".

2.1. Synthesis

The synthesis and single crystals of the studied compounds **2a,b** were prepared as previously reported [19].

(3E,3′E)-3,3′-((Hexane-1,6-diylbis(azanediyl))bis(phenylmethaneylylidene))bis(6-phenyl-2H-pyran-2,4(3H)-dione) **3**

A mixture of pyran-2,4-dione **1** (2.0 mmol) and 1,6-diaminohexane (1.0 mmol) was heated under reflux in methanol (10 mL) for 4 h. Then, it was cooled to room temperature, and the formed precipitate was collected by filtration, dried, and recrystallized from MeOH.

Yield 88%, m.p. 210–211 °C, ^{1}H-NMR (400 MHz, $CDCl_3$; Figures S1 and S2) δ 14.12 (s, 2 H), 7.80 (dd, J = 7.9, 1.2 Hz, 4 H), 7.53–7.51 (m, 6 H), 7.48–7.42 (m, 6 H), 7.26 (dd, J = 7.3, 2.4 Hz, 4 H), 6.44 (s, 2 H), 3.17 (q, J = 6.6 Hz, 4 H), 1.59–1.57 (m, 4 H), 1.31 (s, 4 H); ^{13}C-NMR (101 MHz, $CDCl_3$) δ 185.07, 175.01, 162.07, 160.99, 133.37, 131.29, 131.16, 129.52, 128.93, 128.80, 126.02, 125.82, 125.49, 104.38, 96.87, 45.16, 29.41, 26.07; Elemental analysis (CHN) calculated for [$C_{42}H_{36}N_2O_6$] C, 75.89; H, 5.46; N, 4.21 found C, 75.98; H, 5.60; N, 4.16.

2.2. X-ray Single Crystal Determination of **2a,b** and C_2-Symmetrical Compound **3**

The crystals of **2a,b** and C_2-Symmetrical compound **3** were immersed in cryo-oil, mounted in a loop, and measured at a temperature of 120 K. The X-ray diffraction data were collected on a Rigaku Oxford Diffraction Supernova diffractometer using Cu Kα radiation. The *CrysAlisPro* [26] software package was used for cell refinement and data reduction. A gaussian (**2a**) or multi-scan (**2b**, **3**) absorption correction (*CrysAlisPro* [26]) was applied to the intensities before structure solution. The structure was solved by intrinsic phasing (*SHELXT* [27]) method. Structural refinement was carried out using *SHELXL* [28] software with *SHELXLE* [29] graphical user interface. In compound **2b**, the o-methylphenyl moiety with the NH group was disordered over two sites with the occupancy ratio of 0.83/0.17. Due to the disorder, a rigid-bond restraint (RIGU) was applied to the disordered part of the structure. Furthermore, the carbon atoms of the phenyl rings were fitted to regular hexagons. On the other hand, the OH hydrogen atom in **2a**, N(1)H(1) hydrogen atom in **2b** and NH hydrogen atom in **3** were located from the difference Fourier map and refined isotropically. All other hydrogen atoms were positioned geometrically and constrained to ride on their parent atoms, with C-H = 0.95–0.99 Å, N-H = 0.88, and U_{iso} = 1.2–1.5·U_{eq} (parent atom).

2.3. Hishfeld Analysis

The topology analyses were performed using the Crystal Explorer 17.5 program [30].

3. Results and Discussion

3.1. Synthesis

The synthesis of the target β-enamino-pyran-2,4-diones compounds **2a,b** was achieved by reacting pyran-2,4-dione **1** with *o*-anisidine and *o*-toluidine respectively in methanol [19]. Whereas, C_2-symmetrical *bis*(β-enamino-pyran-2,4-dione) derivative **3** having 1,6-hexylene spacer linking the two β-enamino-pyran-2,4-dione arms was obtained from the reaction of **1** with 1,6-diaminohexane in methanol under reflux for 4 h (Scheme 1). The crystals of the new *bis*(β-enamino-pyran-2,4-dione) derivative **3** and β-enamino-pyran-2,4-diones **2a,b** and **3** were grown in MeOH by slow evaporation at room temperature overnight to afford single crystals suitable for X-ray diffraction analysis.

3.2. Crystal Structure Description of **2a,b** and **3**

The X-ray structure of the studied systems revealed very well the experimentally observed structural characterizations from the spectral analyses. The crystal data and structure refinement details of **2a**, **2b** and **3** are summarized in Table 1. All compounds were crystallized in the triclinic crystal system and the centrosymmetric p-1 space group. All unit cell parameters are listed in the same table. The unit cell comprised two molecular

units in case of **2a** and **2b,** while for **3** there was one molecule per unit cell as the molecule present in the unit cell of **3** lies on an inversion center.

Table 1. Crystal data and structure refinement for the studied compounds **2a**, **2b,** and **3**.

Identification Code	2a	2b	3
empirical formula	$C_{25}H_{19}NO_4$	$C_{25}H_{19}NO_3$	$C_{42}H_{36}N_2O_6$
fw	397.41	381.41	664.73
temp (K)	120(2)	120(2)	120(2)
Λ (Å)	1.54184	1.54184	1.54184
cryst syst	Triclinic	Triclinic	Triclinic
space group	P-1	P-1	P-1
a (Å)	8.4480(2)	8.5656(2)	7.3747(4)
b (Å)	11.3775(3)	11.0766(2)	10.4849(6)
c (Å)	11.4509(3)	11.3943(2)	11.6054(7)
α (°)	62.863(3)	117.766(2)	106.422(5)
β (°)	83.527(2)	93.726(2)	105.512(5)
γ (°)	82.242(2)	93.594(2)	92.416(5)
V (Å^3)	968.87(5)	949.26(4)	822.64(9)
Z	2	2	1
ρcalc (Mg/m^3)	1.362	1.334	1.342
μ (Mo Kα) (mm^{-1})	0.753	0.705	0.726
No. reflns.	21,259	21,678	6894
Unique reflns.	4067	3975	3388
GOOF (F^2)	1.046	1.054	1.045
Rint	0.0238	0.0316	0.0244
R1a ($I \geq 2\sigma$)	0.0323	0.0382	0.0429
wR2b ($I \geq 2\sigma$)	0.0846	0.1024	0.1132
CCDC	2,099,428	2,099,429	2,099,430

The X-ray structure of **2a** along with atom numbering are shown in the left upper part of Figure 1. List of the most important geometrical parameters including bond distance and angles are given in Table S1 (Supplementary Materials). The pyran-2,4-dione moiety is connected directly to a phenyl group where both rings are twisted from each other. The angle between the mean plan passing through the pyran-2,4-dione moiety and the phenyl ring was found to be 24.30°. The structure is stabilized by one intramolecular N1-H1 ... O1 hydrogen bond with donor-acceptor distance of 2.535(1) Å and hydrogen-acceptor distance of 1.732(2) Å, while the N1-H ... O1 angle was 142.7(2)°. As can be seen from the right upper part of Figure 1, each two molecular units formed a dimer via the intermolecular N1-H1 ... O1 hydrogen-bonding interactions with donor-acceptor distance of 2.909(1) Å and hydrogen-acceptor distance of 2.260(2) Å while the N1-H1 ... O1 angle was 126.5(1)°.

The X-ray structure of **2b** along with atom numbering are shown in the lower left part of Figure 1, while the selected bond distance and angles are given in Table S1 (Supplementary Materials). One of the phenyl rings showed disorder over two positions and only the major part is shown in this figure. Additionally, the pyran-2,4-dione moiety connected by phenyl group was found twisted from each other and the twist angle between the mean plan passing through the Pyran-2,4-dione moiety and this phenyl ring was found to be slightly less (21.48°) than that in **2a**. The structure is also stabilized by one intramolecular N1-H1 ... O1 hydrogen bond with N1 ... O1 and H1 ... O1 distances of 2.559(4) Å and 1.738(2) Å, respectively while the N1-H ... O1 angle was 140.26(2)°. As can be seen from the lower left part of Figure 1, each two molecules of **2b** formed a dimer via intermolecular N1-H1 ... O1 hydrogen bonding interactions. In this case, the donor-acceptor distance was 2.883(3) Å and the hydrogen-acceptor distance was 2.173(2) Å while the N1-H ... O1 angle was 129.68(2)°.

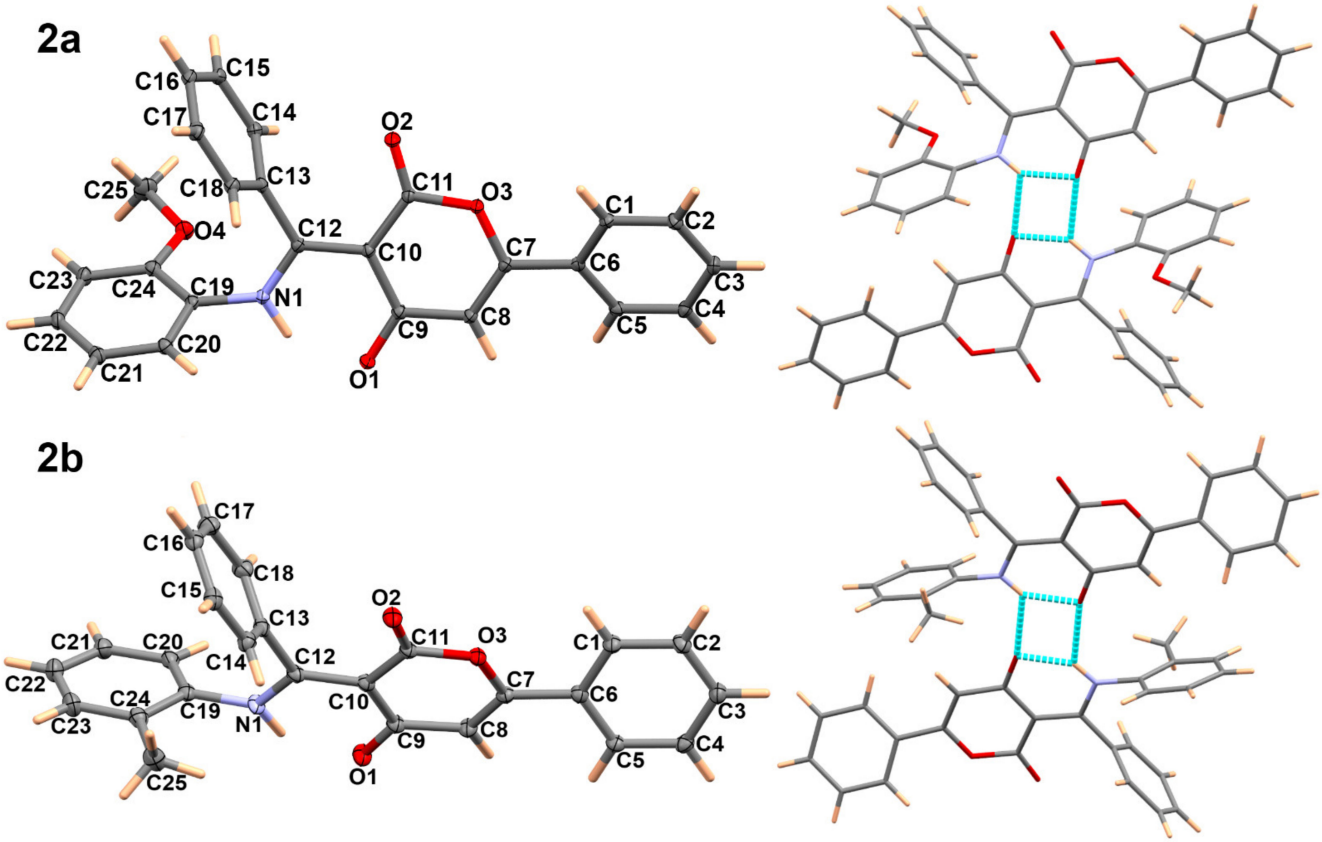

Figure 1. X-ray structures showing atom numbering (**left**) and the dimer formed by the intermolecular hydrogen bonding interactions (**right**) for **2a** and **2b**. The disorder model of compound **2b** is shown in Figure S3 (Supplementary Data) where one of the phenyl rings showed disorder with two parts and only the major part was presented in this figure.

In case of **3**, the molecule exhibited a center of symmetry located at the midpoint of the C21-C21 bond, splitting the molecule into two equivalent halves; hence, the asymmetric unit comprised half molecular unit. Hence, only the atom numbering of half molecule is presented in the lower part of Figure 2. Similar to the other pyran-2,4-dione derivatives, the structure is stabilized by strong intramolecular N1-H1 ... O1 hydrogen bonding interactions with donor-acceptor distance of 2.562(2) Å and hydrogen-acceptor distance of 1.755(2) Å while the N1-H ... O1 angle was 145.57(2)° (Figure 2). Additionally, the twist of the pyran-2,4-dione moiety and the phenyl ring was found to be the highest (31.47°) among the studied systems.

3.3. Analysis of Molecular Packing

The Hirshfeld surfaces of **2a** are shown in Figure S4 (Supplementary Data). Decomposition of the fingerprint plot for all contacts sharing in the crystal stability of **2a** is presented in Figure 3. These fingerprint plots enabled us to determine the percentages of all possible intermolecular contacts affecting the molecular packing in the crystal structure of **2a**. In this plot, the d_e and d_i are the distances from a point on the surface to the nearest nucleus *outside* and *inside* the surface, respectively. The normalized contact distance, (d_{norm}), is defined in terms of d_e, d_i and the vdW radii of the atoms according to Equation (1). It is clear that the H ... H (45.1%), O ... H (19.9%) and H ... C (27.8%) contacts were the most dominant, in addition to some significant contributions from the C ... C (5.2%) and C ... O (1.7%) interactions.

$$d_{norm} = \frac{d_i - r_i^{vdW}}{r_i^{vdW}} + \frac{d_e - r_e^{vdW}}{r_e^{vdW}} \quad (1)$$

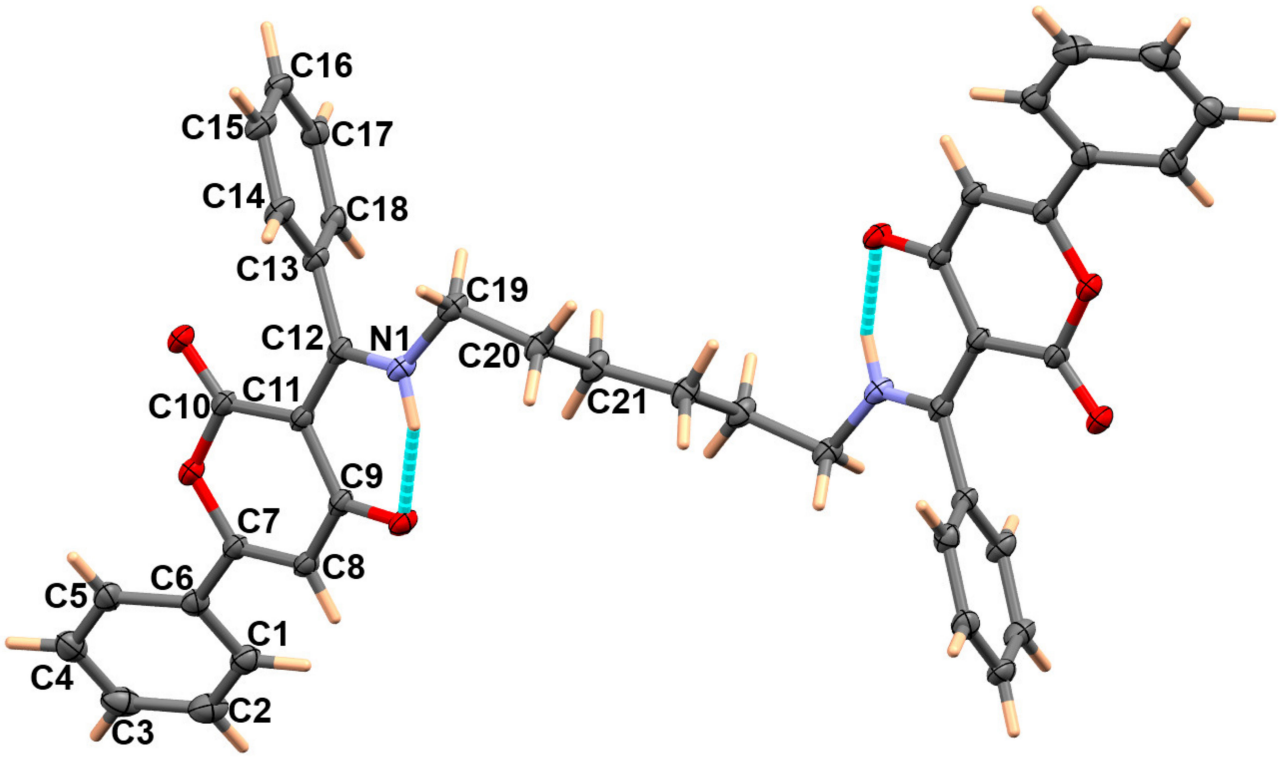

Figure 2. X-ray structure showing atom numbering and the intramolecular hydrogen bonding interactions for C_2-symmetrical compound **3**.

On the other hand, the normalized contact distance (d_{norm}) map yielded good evidence on the important short-contact sharing significantly in the molecular packing (Figure 4). Clear red regions in the d_{norm} map indicate contacts with shorter interaction distances than the vdW radii sum of the interacting atoms. It is clear that many red spots are related to the H . . . H, O . . . H and H . . . C intermolecular interactions, indicating that these contacts are the most significant in the molecular packing of **2a**. Summary of all short contacts and the corresponding interactions distances are listed in Table 2. The shortest H . . . H, O . . . H and H . . . C intermolecular interactions were H4 . . . H14, H25B . . . C5 and O1 . . . H1 contacts having interaction distances of 2.142, 2.702, and 2.212 Å, respectively.

Additionally, the results indicated some C . . . C contacts (5.2%) belong to the π-π stacking interactions, which were further revealed by the presence of a large green flat area in the curvedness and the complementary red/blue triangles in the shape index (Figure 5). The shortest C . . . C contacts were C11 . . . C5 and C11 . . . C4 with interaction distances of 3.287 and 3.227 Å, respectively.

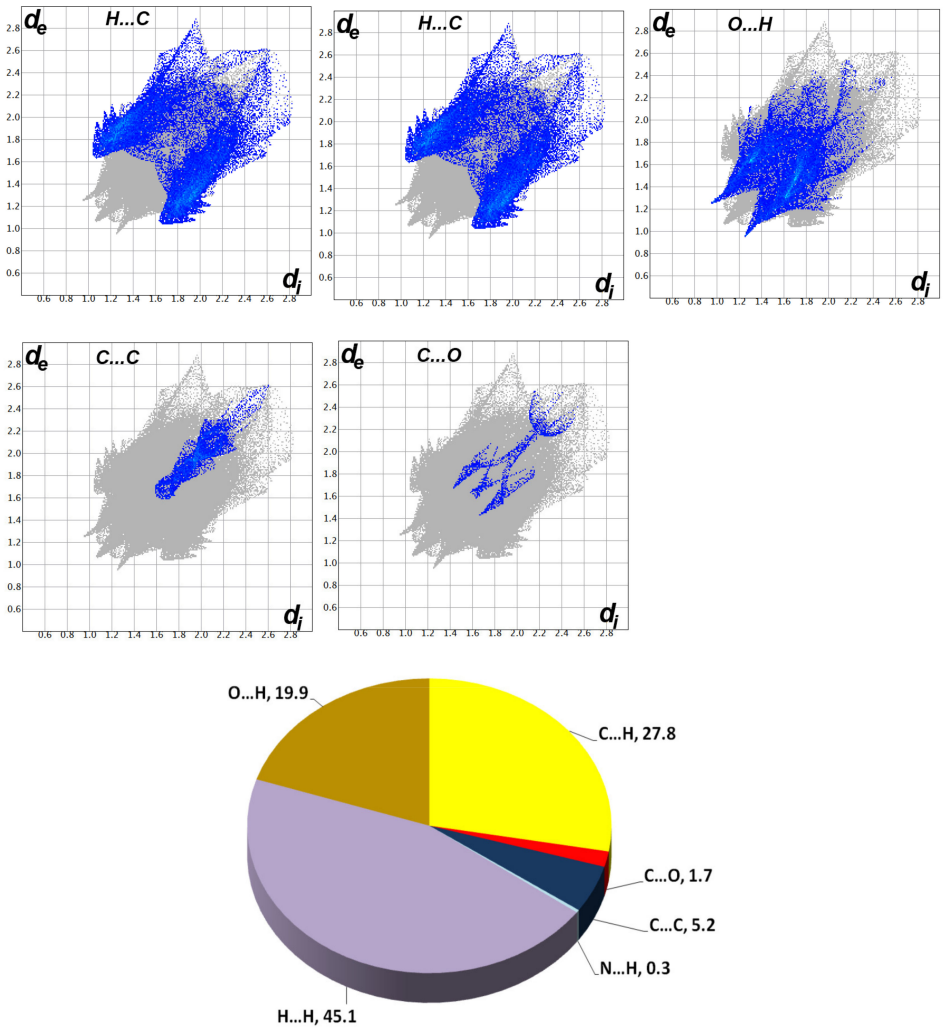

Figure 3. Decomposed fingerprint plots of the most dominant contacts and pie chart showing the percentages of all possible intermolecular interactions in the crystal structure of **2a**.

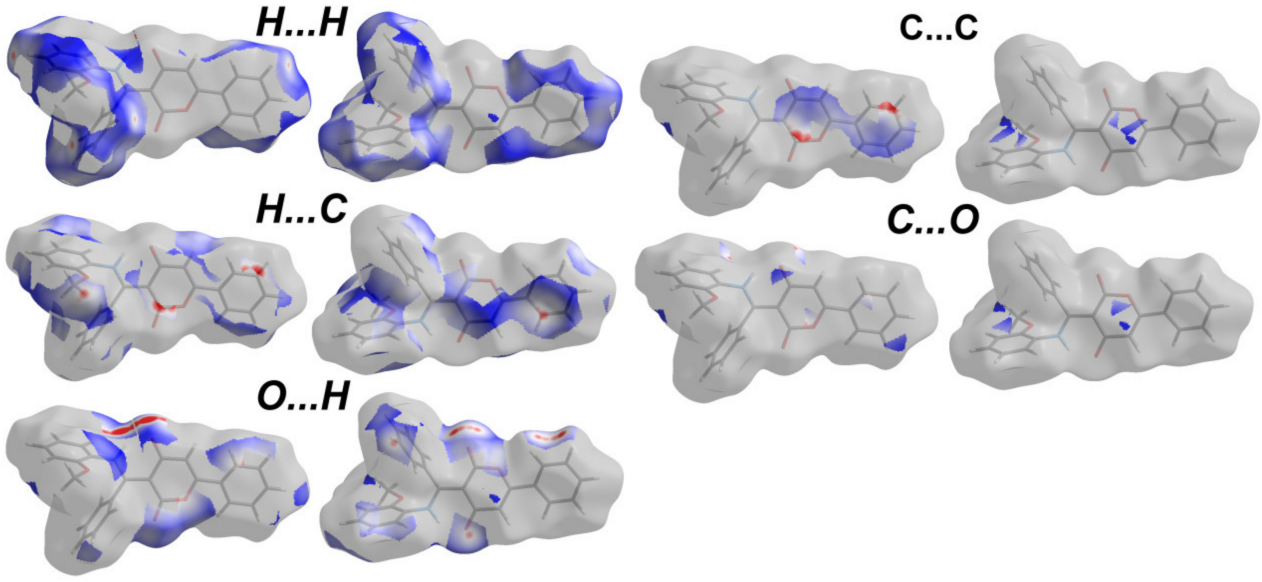

Figure 4. Decomposed d_{norm} maps of the most important contacts in **2a**.

Table 2. Most important contacts and the corresponding shortest interaction distances.

Contact	Distance	Contact	Distance
H25B . . . C5	2.702	H15 . . . H22	2.274
H25B . . . C6	2.761	H4 . . . H14	2.142
C1 . . . O1	3.099	O2 . . . H2	2.436
C11 . . . C5	3.287	O2 . . . H1A	2.512
C11 . . . C4	3.227	O1 . . . .H17	2.537
C10 . . . .C4	3.563	O1 . . . H1	2.212

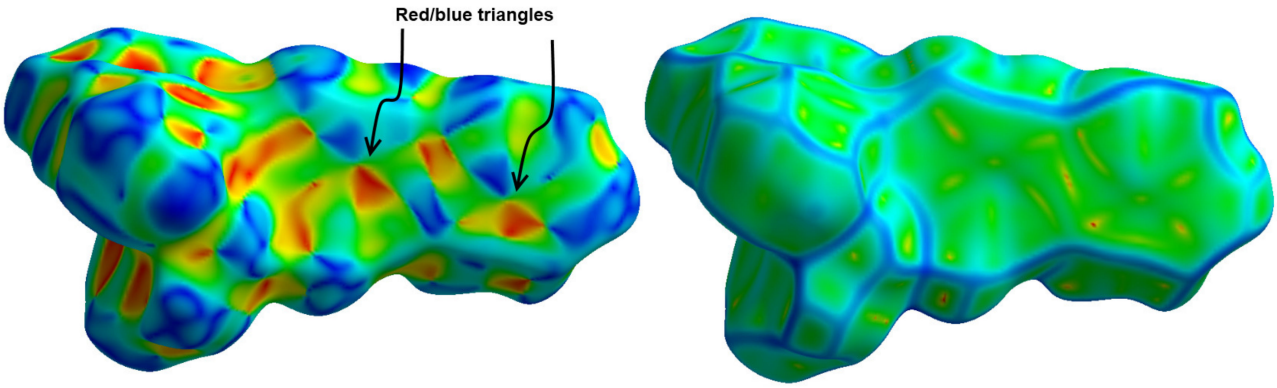

Figure 5. Shape index (**left**) and curvedness (**right**) revealed the π-π interactions in **2a**.

For **2b**, the Hirshfeld surfaces showing the d_{norm}, shape index and curvedness maps are presented in Figure S5 (Supplementary Data). Decomposition of the fingerprint plot for all contacts sharing in the crystal stability of **2b** is presented in Figure 6. Based on the decomposed fingerprint plots, the most abundant contacts were the H . . . H, O . . . H and H . . . C interactions. Their percentages were calculated to be 47.2%, 17.5%, and 28.1% from the whole intermolecular contacts affecting the molecular packing in the crystal structure of **2b**. In addition, some significant contributions from the C . . . C (5.2%) and C . . . O (1.6%) interactions were detected.

Additionally, the decomposed d_{norm} maps were used to locate the regions sharing significant interactions with the neighboring molecular units (Figure 7). Based on the decomposed d_{norm} maps, all contacts having shorter distances than the vdWs radii sum of the interacting atoms are collected in Table 3. Additionally, the corresponding interaction distances are depicted in the same table. It is clear that the H . . . H interactions occurred at longer distances (2.420 Å; H15 . . . H22) compared with **2a**. In contrast, the H . . . C interactions occurred at shorter distances (2.629 Å; H22 . . . C15) compared with **2a**. Similarly, the shortest O . . . H contact (O1 . . . H1; 2.144 Å) occurred at a shorter distance compared with **2a**. As can be seen from the shape index and curvedness maps, the characteristic features of the π-π stacking interactions are evident (Figure S5 (Supplementary Data)). The shortest C . . . C contacts were C4 . . . C11 and C4 . . . C10, while the corresponding interaction distances were 3.232 and 3.350 Å, respectively.

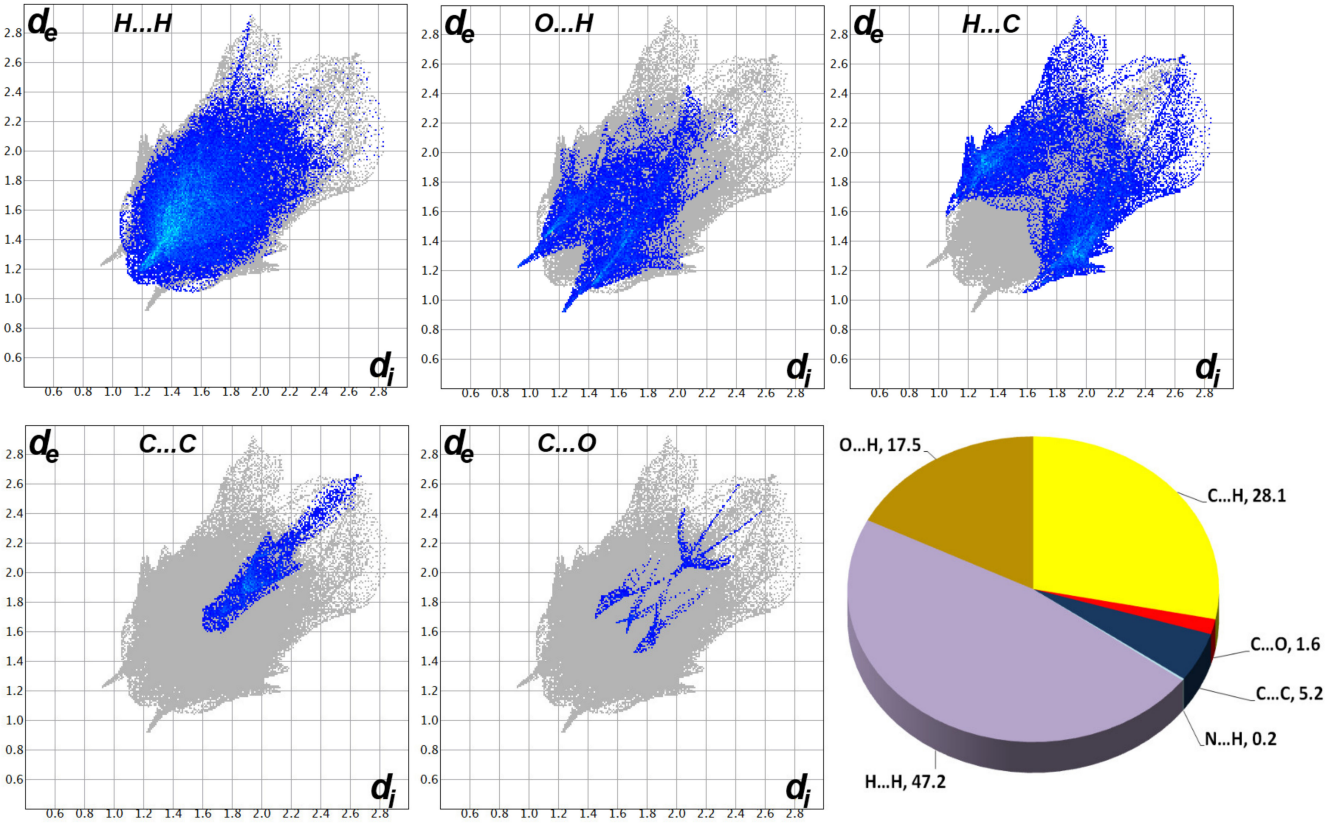

Figure 6. Decomposed fingerprint plots of the most dominant contacts and pie chart showing the percentages of all possible intermolecular interactions in the crystal structure of **2b** (major part).

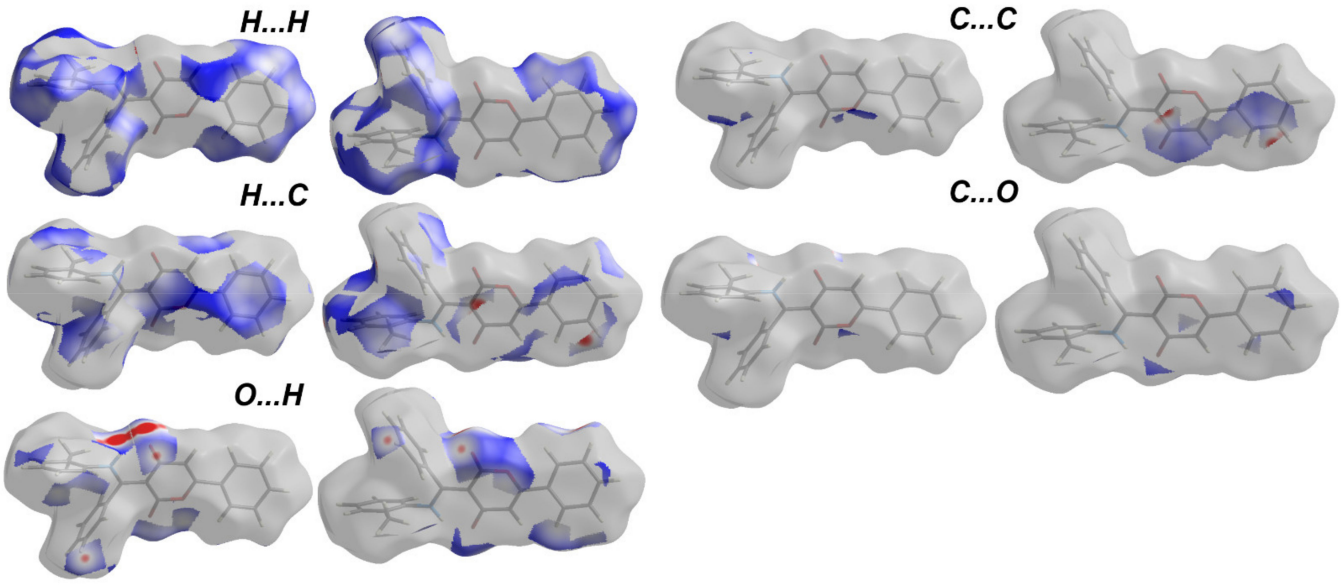

Figure 7. Decomposed d_{norm} maps of the most important contacts in **2b** (major part).

Table 3. Most important contacts and the corresponding shortest interaction distances.

Contact	Distance	Contact	Distance
H22 . . . C15	2.629	O2 . . . H15	2.526
C4 . . . C10	3.350	O1 . . . H17	2.523
C4 . . . C11	3.232	O1 . . . H1	2.144
H15 . . . H22	2.420	O2 . . . H2	2.383
		O3 . . . H21	2.581

The Hirshfeld surfaces of the C_2-symmetrical compound **3** are shown in Figure S6 (Supplementary Data). Additionally, the dominant interactions in this compound were H . . . H (46.4%), H . . . C (28.7%) and O . . . H (20.2%) contacts based on the decomposed fingerprint plots (Figure 8). Similar to **2b**, there were no red regions in the d_{norm} map corresponding to the H . . . H contacts (Figure 8). The opposite was true for the O . . . H and H . . . C contacts. The O . . . H interactions appeared as more sharp spikes in the fingerprint plot compared with the H . . . C ones. Hence, the O . . . H interactions were more significant in the molecular packing compared with the H . . . C contacts. List of the short intermolecular contacts are depicted in Table 4. Additionally, the results indicated a contribution of 2.4% for the C . . . C contacts where the C4 . . . C5 was the shortest (3.348 Å), indicating the presence of some weak π-π stacking interactions.

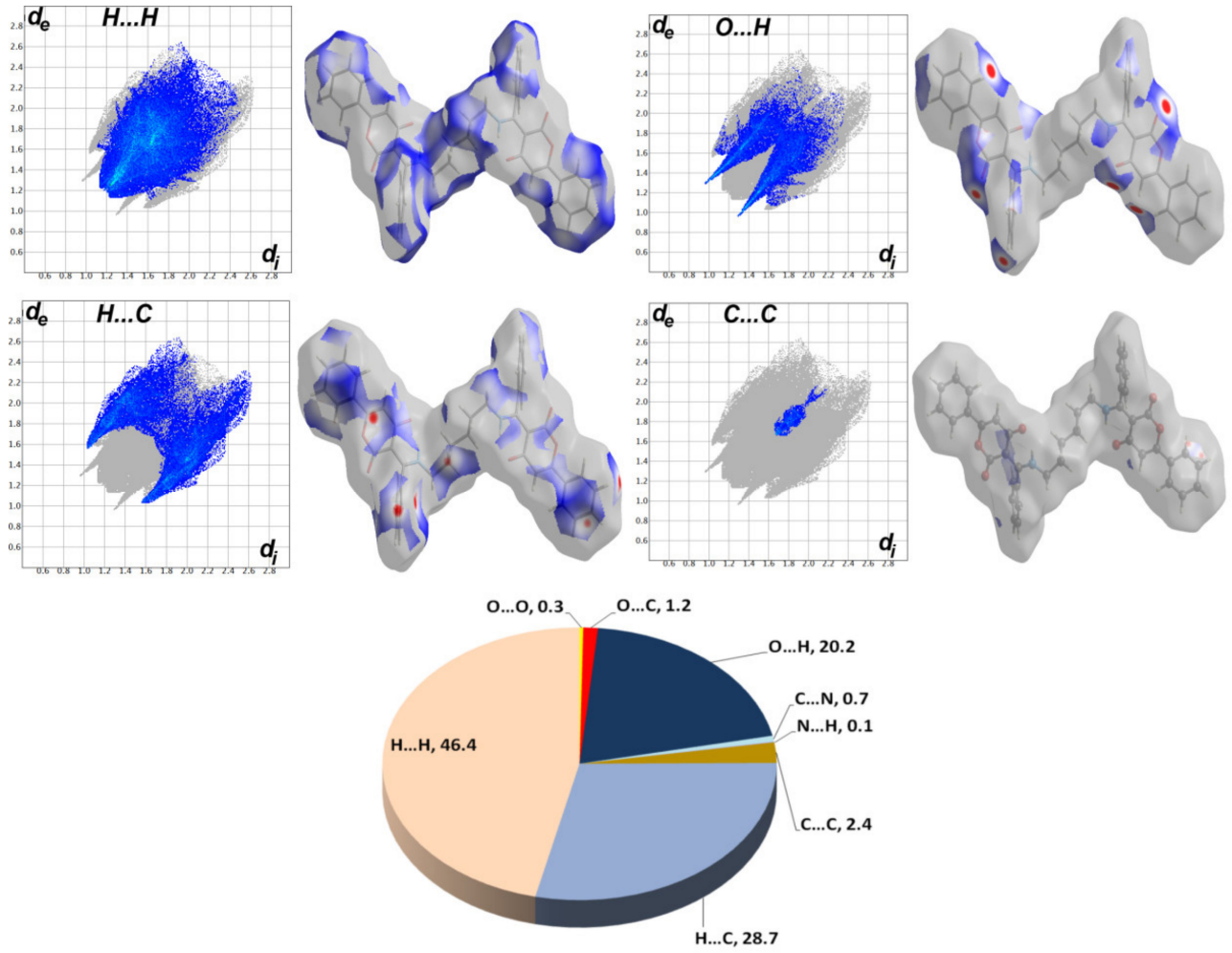

Figure 8. Decomposed fingerprint plots and d_{norm} maps of the most dominant contacts and pie chart showing the percentages of all possible intermolecular interactions in the crystal structure of the C_2-symmetrical compound **3**.

Table 4. Most important contacts and the corresponding shortest interaction distances.

Contact	Distance	Contact	Distance
H21B . . . C2	2.784	O2 . . . H1A	2.345
H21B . . . C3	2.689	O2 . . . H16	2.407
H4 . . . C17	2.589	O3 . . . H11	2.261
H4 . . . C18	2.736	C4 . . . C5	3.348
H17 . . . C7	2.624		

3.4. DFT Studies

The structures of the studied compounds were calculated starting from their X-ray structures and the resulting optimized geometries are depicted in Figure 9 (left part) while the right part of the same figure shows the overlay between the calculated and experimental structures. Generally, the calculated structures showed good agreements with the experimentally observed X-ray structures. Some deviations between the calculated and experimental structures could be attributed to the crystal packing effects. Comparison between the calculated and experimental bond distances and angles are shown in Table S2 (Supplementary Data). In Figure 10, there are very good straight line correlations (R^2 = 0.913–0.982) between the calculated and experimental geometric parameters. The good correlations with high R^2 values between the calculated and experimental geometrical parameters present an accurate mathematical expression relating them.

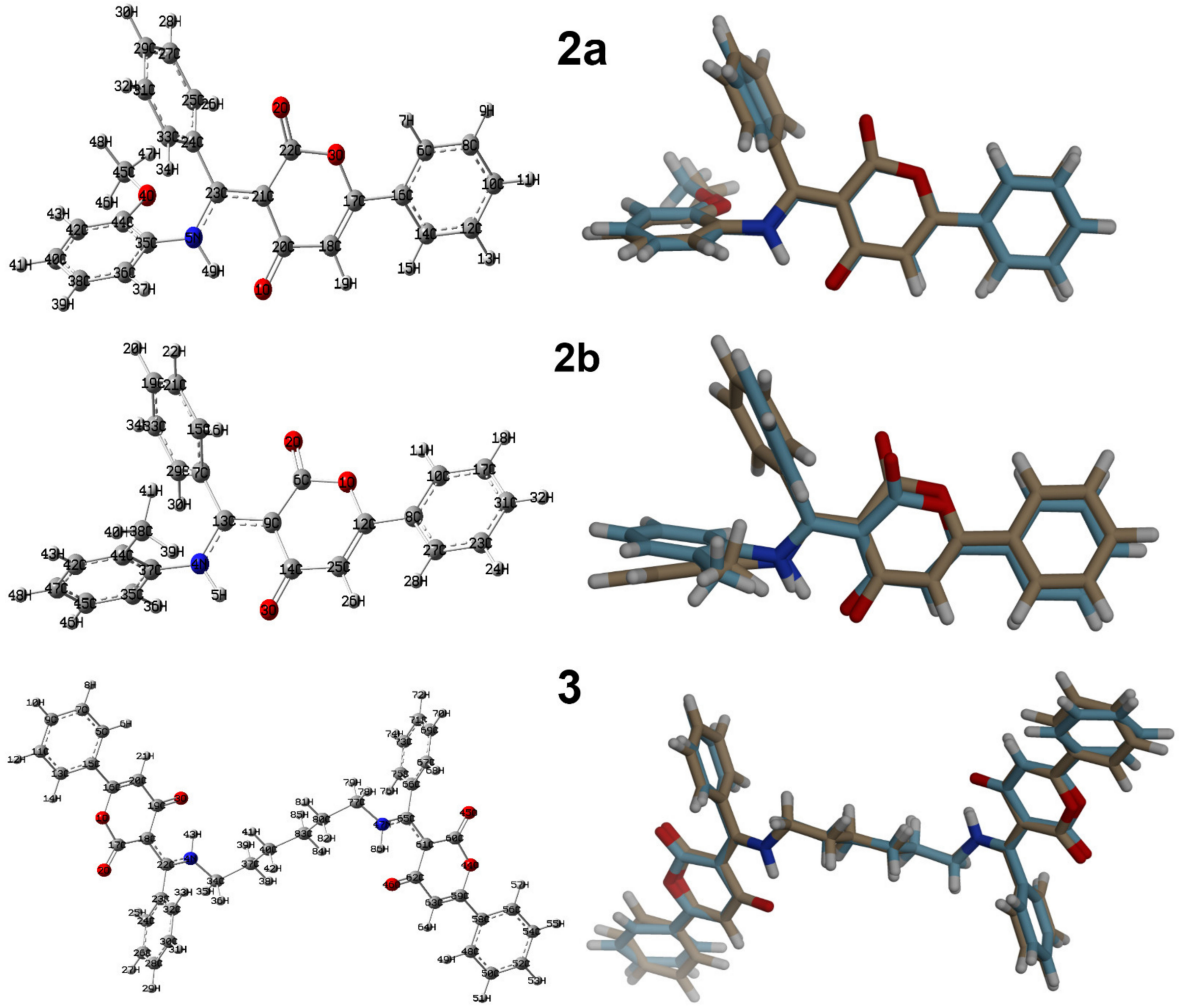

Figure 9. The optimized geometry (**left**) and overlay of the optimized with experimental structures, (**right**) for the studied compounds.

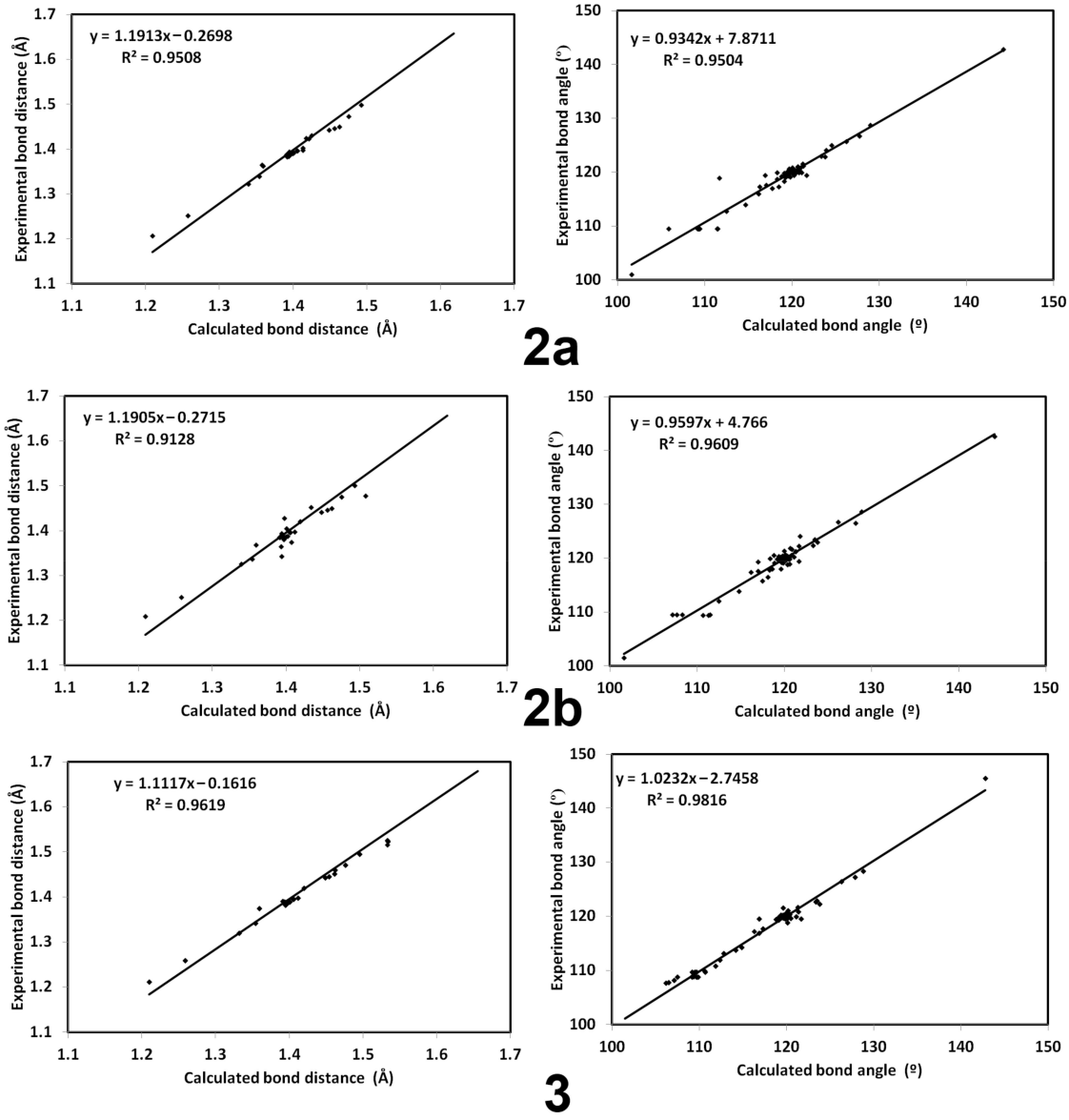

Figure 10. The straight line correlations between the calculated and experimental geometric parameters.

The studied systems comprised the CHNO backbone where the charge distribution at the different atomic sites has a direct impact on the molecular reactivity and electronic properties of the molecular systems. The calculated natural charges at different atomic sites are presented graphically in Figure 11. The results presented clear evidence on the electronegative nature of the nitrogen, oxygen, and the majority of carbon atoms where the carbonyl oxygen atoms had the highest negative charge. The calculated natural charges at the carbonyl oxygen were −0.578 to −0.641, −0.577 to −0.643, and −0.580 to −0.653 e for compounds **2a**, **2b**, and **3**, respectively. The corresponding values for the ether oxygen atom are −0.526 to −0.518, −0.525, and −0.525, respectively. On the other hand, the secondary amine nitrogen atom had less negative natural charges than the carbonyl oxygen atom and more negative natural charge than the ether oxygen atom. The natural charges at the N-atom of the amino group were calculated to be −0.563, −0.570, and −0.557 e for compounds **2a**, **2b**, and **3**, respectively. Additionally, the majority of carbon atoms had a negative charge except those attached to the N or O atoms. All carbon atoms bonded to nitrogen or oxygen were positively charged. As expected, the hydrogen atoms were positively charged where the NH proton was the most positive among hydrogen sites. The NH proton had natural charges of 0.476, 0.475, and 0.464 e for compounds **2a**, **2b**, and **3**,

respectively. Additionally, the oxygen atom of the carbonyl directly attached to the ether oxygen had the most positive charge compared with the other atomic sites. The calculated natural charges at the carbonyl carbon were calculated to be 0.794, 0.793 and 0.792 e, respectively. The studied compounds (except **3**) were polar with net dipole moments of 3.540 and 2.110 Debye for compounds **2a** and **2b**, respectively. In contrast, compound **3** was non polar with zero net dipole moment due to the presence of an inversion center, as it has the c_i point group. The direction of the dipole moment vector is shown over the molecular electrostatic potential (MEP) map in Figure 12.

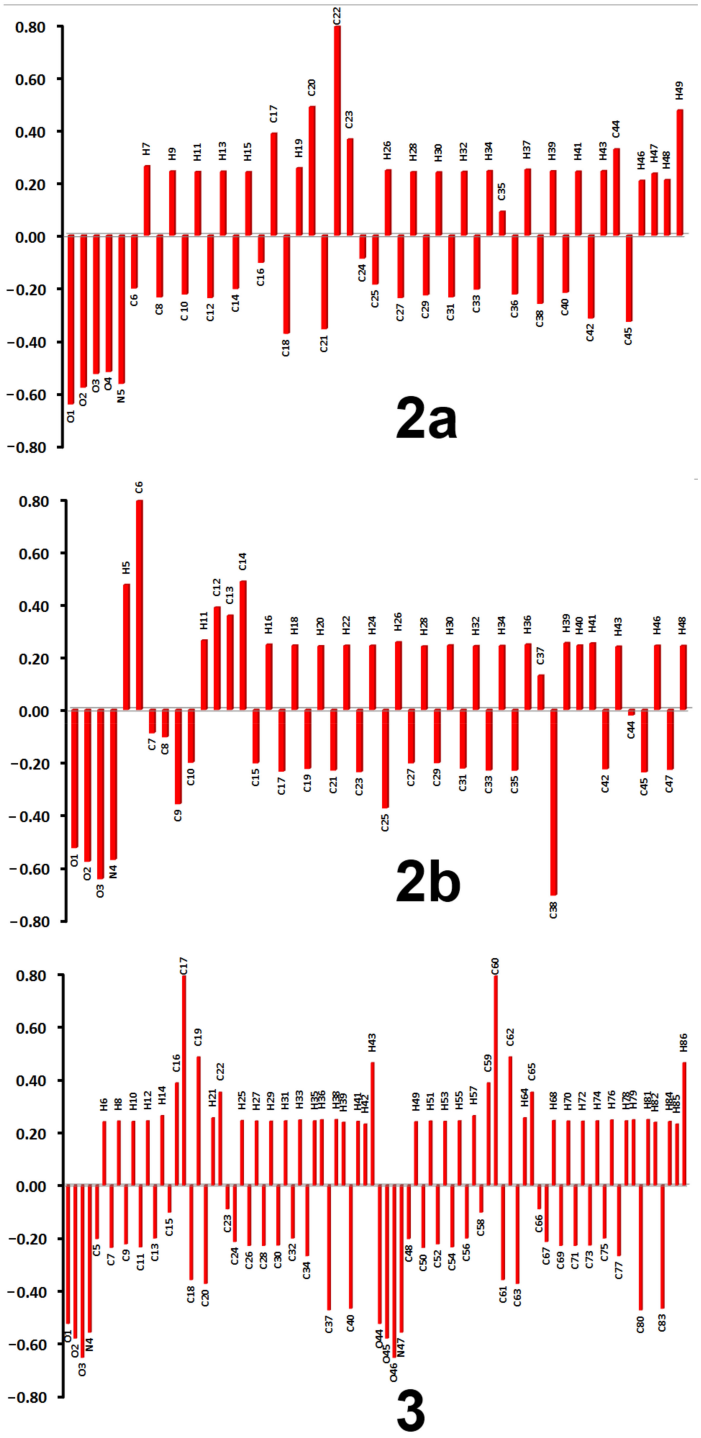

Figure 11. Natural charge populations at the different atomic sites for the studied compounds.

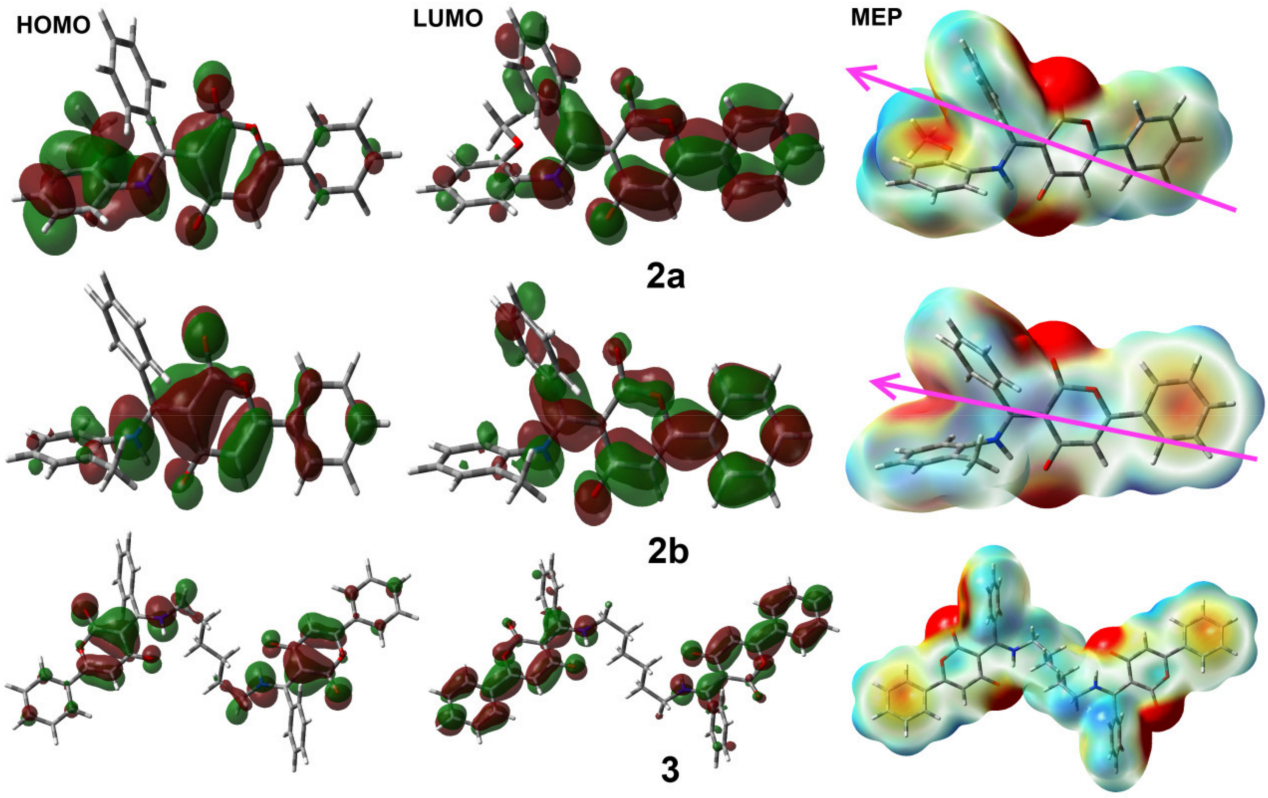

Figure 12. The MEP, HOMO, and LUMO for the studied compounds. In MEP the red and blue colors indicate the most negative and most positive regions, respectively.

In MEP maps shown in Figure 12, the high electron density related to the carbonyl oxygen atoms is clearly evident from the red regions close to these sites. In contrast, the high positive charge density of the NH proton could not be clearly seen from the presented MEP maps due to its proximity to the carbonyl oxygen which has an intense red region around it. In any case, the values of the electron density at the NH proton were positive around this atomic site. Hence, the NH group could be considered as the most suggested group as hydrogen bond donor while the carbonyl oxygen atom is the most suitable hydrogen bond-acceptor site. These results are in accordance with the observed X-ray structure of the studied system.

Additionally, the HOMO and LUMO levels are presented in Figure 12. It is clear that the HOMO and LUMO levels were mainly located over the π-system of the studied molecules. Hence the HOMO-LUMO intramolecular charge transfer could be described mainly as a π-π* transition. The HOMO and LUMO energies are important parameters for calculating molecular reactivity parameters such as ionization potential ($I = -E_{HOMO}$), electron affinity ($A = -E_{LUMO}$), chemical potential ($\mu = -(I + A)/2$), and hardness ($\eta = (I-A)/2$), as well as electrophilicity index ($\omega = \mu^2/2\eta$) [31–36]. The energies of the HOMO and LUMO levels were the highest for **2a** while they were the lowest for **2b**. Hence, the ionization potential and electron affinity values of **2a** were the lowest and were the highest for **2b**. Additionally, **2a** had the lowest hardness and the highest chemical potential. The order of the electrophilic characters, as indicated from the electrophilicity index (ω), is **2a** > **3** > **2b** (Table 5).

3.5. NMR Spectra

NMR chemical shifts for the protons and carbons were calculated using the GIAO method and the results are tabulated in Tables S3–S5 (Supplementary Data). Correlations between the experimental and theoretical results are presented in Figure 13. As shown from these correlation graphs, the correlation coefficients (R^2) were high and close to 1. The R^2

values ranged from 0.9827–0.9948 and 0.9547–0.9868 for ^{1}H- and ^{13}C-NMR chemical shifts, respectively. These results indicated that there is good agreement between the experimental and theoretical results.

Table 5. Reactivity parameters of the studied compounds.

Parameter	2a	2b	3
E_{HOMO}	−5.8214	−5.9912	−5.9357
E_{LUMO}	−1.8452	−1.9173	−1.8545
I	5.8214	5.9912	5.9357
A	1.8452	1.9173	1.8545
η	3.9762	4.0738	4.0812
μ	−3.8333	−3.9543	−3.8951
ω	1.8478	1.9191	1.8587

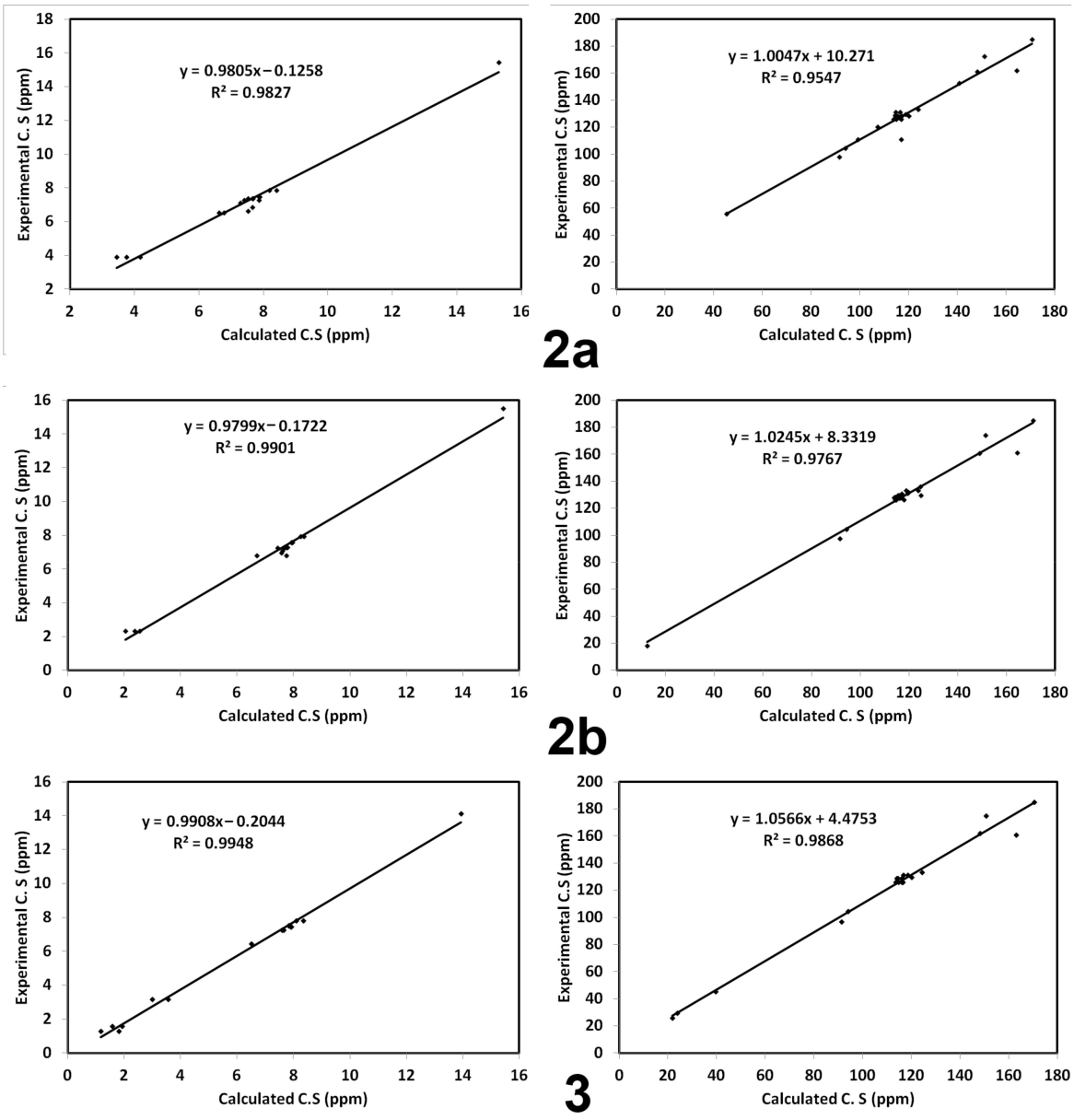

Figure 13. ^{1}H- and ^{13}C-NMR correlations between the calculated and experimental data.

4. Conclusions

In conclusion, the synthesis of a new C_2-symmetrical *bis*(*β*-enamino-pyran-2,4-dione) derivative **3** was achieved. X-Ray single crystal structures of **2a,b** and **3** were developed and, hence, structures unambiguously determined. The supramolecular structures of the studied compounds were analyzed using Hirshfeld calculations. All structures were optimized and the calculated structures were in good agreement with the experimentally observed X-ray crystal structures. At the optimized geometry of each compound, the electronic parameters were calculated and compared. Additionally, the calculated NMR chemical shifts were in good agreement with the experimental data. The possible applications of the synthesised C_2-symmetrical *bis*(*β*-enamino-pyran-2,4-dione) derivative **3** and mono-derivative **2a,b** will be considered in the near future.

Supplementary Materials: The following are available online at https://www.mdpi.com/article/10.3390/sym13091646/s1, X-ray single crystal determination of **1**; Figures S1 and S2:^{1}H-NMR and ^{13}C-NMR of **3** in $CDCl_3$; Figure S3: X-ray structure of compound **2b** showing the disordered phenyl ring. Figures S4–S6: Hirshfeld surfaces of **2a,b** and **3**. Table S1. Selected bond lengths [Å] and angles [°] for the studied compounds. Table S2: List of calculated and experimental bond distances and angles. Tables S2–S4 The calculated chemical shifts of **2a,b** and **3**.

Author Contributions: Conceptualization, A.T.A.B., S.M.S. and A.B.; synthesis and characterization, A.T.A.B., A.A.M.S. and A.M.A.-M.; X-ray crystal structure carried out by: M.H.; writing original manuscript, A.T.A.B., S.M.S. and A.B.; revision and editing, A.T.A.B., S.M.S. and A.B. All authors have read and agreed to the published version of the manuscript.

Funding: Researchers Supporting Project (RSP-2021/64), King Saud University, Riyadh, Saudi Arabia.

Institutional Review Board Statement: Not applicable.

Informed Consent Statement: Not applicable.

Data Availability Statement: Not applicable.

Acknowledgments: The authors would like to extend their sincere appreciation to the Researchers Supporting Project (RSP-2021/64), King Saud University, Riyadh, Saudi Arabia.

Conflicts of Interest: The authors declare no conflict of interest.

References

1. Rateb, M.E.; Ebel, R. Secondary metabolites of fungi from marine habitats. *Nat. Prod. Rep.* **2011**, *28*, 290–344. [CrossRef] [PubMed]
2. Lee, I.-K.; Yun, B.-S. Styrylpyrone-class compounds from medicinal fungi *Phellinus* and *Inonotus* spp., and their medicinal importance. *J. Antibiot.* **2011**, *64*, 349–359. [CrossRef] [PubMed]
3. Lee, J.S. Recent advances in the synthesis of 2-pyrones. *Mar. Drugs* **2015**, *13*, 1581–1620.
4. McGlacken, G.P.; Fairlamb, I.J.S. 2-Pyrone natural products and mimetics: Isolation, characterisation and biological activity. *Nat. Prod. Rep.* **2005**, *22*, 369–385. [CrossRef]
5. Nagai, K.; Kamigiri, K.; Matsumoto, H.; Kawano, Y.; Yamaoka, M.; Shimoi, H.; Watanabe, M.; Suzuki, K. YM-202204, a new antifungal antibiotic produced by marine fungus *Phoma* sp. *J. Antibiot.* **2002**, *55*, 1036–1041. [CrossRef]
6. Zhang, Y.; Li, C.; Swenson, D.C.; Gloer, J.B.; Wicklow, D.T.; Dowd, P.F. Novel antiinsectan oxalicine alkaloids from two undescribed fungicolous *Penicillium* spp. *Org. Lett.* **2003**, *5*, 773–776. [CrossRef]
7. Nair, M.G.; Chandra, A.; Thorogood, D.L. Griseulin, a new nitro-containing bioactive metabolite produced by *Streptomyces* spp. *J. Antibiot.* **1993**, *46*, 1762–1763. [CrossRef] [PubMed]
8. Sitachitta, N.; Gadepalli, M.; Davidson, B.S. New *α*-pyrone-containing metabolites from a marine-derived actinomycete. *Tetrahedron* **1996**, *52*, 8073–8080. [CrossRef]
9. Kalaitzis, J.A.; Cheng, Q.; Thomas, P.M.; Kelleher, N.L.; Moore, B.S. In vitro biosynthesis of unnatural enterocin and wailupemycin polyketides. *J. Nat. Prod.* **2009**, *72*, 469–472. [CrossRef]
10. Nair, M.S.R.; Carey, S.T. Metabolites of phyrenomycetes II: Nectriapyrone, an antibiotic monoterpenoid. *Tetrahedron Lett.* **1975**, *16*, 1655–1658. [CrossRef]
11. Fu, P.; Liu, P.; Qu, H.; Wang, Y.; Chen, D.; Wang, H.; Li, J.; Zhu, W. *α*-Pyrones and diketopiperazine derivatives from the marine-derived actinomycete *Nocardiopsis dassonvillei* HR10-5. *J. Nat. Prod.* **2011**, *74*, 2219–2223. [CrossRef]
12. Kim, M.C.; Kwon, O.W.; Park, J.S.; Kim, S.Y.; Kwon, H.C. Nocapyrones H-J, 3,6-disubstituted *α*-pyrones from the marine actinomycete *Nocardiopsis* sp. KMF-001. *Chem. Pharm. Bull.* **2013**, *61*, 511–515. [CrossRef] [PubMed]

13. Kim, Y.; Ogura, H.; Akasaka, K.; Oikawa, T.; Matsuura, N.; Imada, C.; Yasuda, H.; Igarashi, Y. Nocapyrones: α- and γ-pyrones from a marine-derived *Nocardiopsis* sp. *Mar. Drugs* **2014**, *12*, 4110–4125. [CrossRef] [PubMed]
14. Graziani, E.I.; Ritacco, F.V.; Bernan, V.S.; Telliez, J.-B. Phaeochromycins A–E, anti-inflammatory polyketides isolated from the soil actinomycete *Streptomyces phaeochromogenes* LL-P018. *J. Nat. Prod.* **2005**, *68*, 1262–1265. [CrossRef]
15. Zhang, J.; Jiang, Y.; Cao, Y.; Liu, J.; Zheng, D.; Chen, X.; Han, L.; Jiang, C.; Huang, X. Violapyrones A–G, α-pyrone derivatives from *Streptomyces violascens* isolated from *Hylobates hoolock* feces. *J. Nat. Prod.* **2013**, *76*, 2126–2130. [CrossRef] [PubMed]
16. Shin, H.J.; Lee, H.S.; Lee, J.S.; Shin, J.; Lee, M.A.; Lee, H.S.; Lee, Y.J.; Yun, J.; Kang, J.S. Violapyrones H and I, new cytotoxic compounds isolated from *Streptomyces* sp. associated with the marine starfish *Acanthaster planci*. *Mar. Drugs* **2014**, *12*, 3283–3291. [CrossRef] [PubMed]
17. Stout, E.P.; Hasemeyer, A.P.; Lane, A.L.; Davenport, T.M.; Engel, S.; Hay, M.E.; Fairchild, C.R.; Prudhomme, J.; le Roch, K.; Aalbersberg, W.; et al. Antibacterial neurymenolides from the fijian red alga *Neurymenia fraxinifolia*. *Org. Lett.* **2008**, *11*, 225–228. [CrossRef]
18. Liu, D.; Li, X.M.; Meng, L.; Li, C.S.; Gao, S.S.; Shang, Z.; Proksch, P.; Huang, C.G.; Wang, B.G. Nigerapyrones A–H, alpha-pyrone derivatives from the marine mangrove-derived endophytic fungus *Aspergillus niger* MA-132. *J. Nat. Prod.* **2011**, *74*, 1787–1791. [CrossRef]
19. Sarhan, A.A.; Haukka, M.; Barakat, A.; Boraei, A.T. A novel synthetic approach to pyran-2,4-dione scaffold production: Microwave-assisted dimerization, cyclization, and expeditious regioselective conversion into β-enamino-pyran-2, 4-diones. *Tetrahedron Lett.* **2020**, *61*, 152660. [CrossRef]
20. Xue, F.; Li, X.; Wan, B. A class of benzene backbone-based olefin-sulfoxide ligands for Rh-catalyzed enantioselective addition of arylboronic acids to enones. *J. Org. Chem.* **2011**, *76*, 7256–7262. [CrossRef]
21. Gianni, J.; Pirovano, V.; Abbiati, G. Silver triflate/p-TSA co-catalysed synthesis of 3-substituted isocoumarins from 2-alkynylbenzoates. *Org. Biomol. Chem.* **2018**, *16*, 3213–3219. [CrossRef]
22. Thibonnet, J.; Abarbri, M.; Parrain, J.L.; Duchene, A. One-step synthesis of alpha-pyrones from acyl chlorides by the Stille reaction. *J. Org. Chem.* **2002**, *67*, 3941–3944. [CrossRef]
23. Chaladaj, W.; Corbet, M.; Furstner, A. Total synthesis of neurymenolide a based on a gold-catalyzed synthesis of 4-hydroxy-2-pyrones. *Angew. Chem. Int. Ed.* **2012**, *51*, 6929–6933. [CrossRef]
24. Lee, J.S.; Shin, J.; Shin, H.J.; Lee, H.-S.; Lee, Y.-J.; Lee, H.-S.; Won, H. Total synthesis and configurational validation of (+)-violapyrone C. *Eur. J. Org. Chem.* **2014**, *2014*, 4472–4476. [CrossRef]
25. Yeh, P.-P.; Daniels, D.S.B.; Cordes, D.B.; Slawin, A.M.Z.; Smith, A.D. Isothiourea-mediated one-pot synthesis of trifluoromethyl substituted 2-pyrones. *Org. Lett.* **2014**, *16*, 964–967. [CrossRef]
26. Rikagu Oxford Diffraction. *CrysAlisPro*; Agilent Technologies Inc.: Yarnton, UK, 2018.
27. Sheldrick, G.M. SHELXT–Integrated space-group and crystal-structure determination. *Acta Cryst.* **2015**, *A71*, 3–8. [CrossRef]
28. Sheldrick, G.M. Crystal structure refinement with SHELXL. *Acta Cryst.* **2015**, *C71*, 3–8.
29. Hübschle, C.B.; Sheldrick, G.M.; Dittrich, B. ShelXle: A Qt graphical user interface for SHELXL. *J. Appl. Cryst.* **2011**, *44*, 1281–1284. [CrossRef]
30. Turner, M.J.; McKinnon, J.J.; Wolff, S.K.; Grimwood, D.J.; Spackman, P.R.; Jayatilaka, D.; Spackman, M.A. Crystal Explorer17 University of Western Australia. 2017. Available online: http://hirshfeldsurface.net (accessed on 12 June 2017).
31. Foresman, J.B.; Frisch, E. *Exploring Chemistry with Electronic Structure Methods*, 2nd ed.; Gaussian: Pittsburgh, PA, USA, 1996.
32. Chang, R. *Chemistry*, 7th ed.; McGraw-Hill: New York, NY, USA, 2001.
33. Kosar, B.; Albayrak, C. Spectroscopic investigations and quantum chemical computational study of (E)-4-methoxy-2-[(p-tolylimino) methyl] phenol. *Spectrochim. Acta* **2011**, *78*, 160–167. [CrossRef]
34. Koopmans, T.A. Ordering of wave functions and eigenenergies to the individual electrons of an atom. *Physica* **1933**, *1*, 104–113. [CrossRef]
35. Parr, R.G.; Yang, W. *Density-Functional Theory of Atoms and Molecules*; Oxford University Press: New York, NY, USA, 1989.
36. Parr, R.G.; Szentpaly, L.V.; Liu, S. Electrophilicity index. *J. Am. Chem. Soc.* **1999**, *121*, 1922–1924. [CrossRef]